Intermolecular charge transfer in electron-deficient MOF to enhance NIR absorption for photothermal conversion and water evaporation

Hao Zeng,[a,b] Ci Kong,[a,b] Jianqi Xiong,[a] Chixian He,[a] Shubiao Xia,[a] Jian-Jun Liu*[a]*

[a]*Yunnan Key Laboratory of Crystalline Porous Organic Functional Materials, College of Chemical and Materials Engineering, Qujing Normal University, Qujing 655011, China*

[b]*Yunnan Key Laboratory of Chiral Functional Substance Research and Application, Yunnan Minzu University, Kunming 650504, China.*

E-mail: xiashubiao401@163.com (S. Xia); jjliu302@163.com (J.-J Liu).

1. General methods

All air- and moisture-sensitive solutions and chemicals were handled under an argon atmosphere. Anhydrous solvents were purchased from Sigma-Aldrich and used without further purification. Unless otherwise stated, all reagents were commercially available and used as received without further purification. Chemicals were obtained from Sigma-Aldrich, Acros, TCI and Alfa-Aesar. Powder X-ray diffraction (XRD) measurements was recorded on a Bruker D8 ADVANCE X-Ray diffractometer at room temperature using a graphite monochromator Cu-target tube. UV-Vis-NIR spectra were performed on a Varian Cary UV-Vis-NIR spectrophotometer. Thermostability of materials were performed on a Mettler Toledo TGA2 thermogravimetric system at N_2 atmosphere from 30 to 800 °C with a ramp rate of 10 °C/min. Electron paramagnetic resonance (EPR) spectra were recorded on a Bruker A300 ESR spectrometer. ^{13}C solid-state nuclear magnetic resonance (^{13}C NMR) spectra were recorded on a Bruker Avance Neo 400WB.

2. Experimental section

2.1 Synthesis of DPNDI

DPNDI was synthesized according to the methods of literature [S1].

2.2 Synthesis of Zn-NDI

Zn-NDI was prepared according to our previously published method [S2]. In a test tube (12 × 1 cm), a mixture solution (0.5 mL) of *N*-methyl-2-pyrrolidone (NMP) and ethanol (NMP/EtOH, 1:1, v/v) was carefully layered on an NMP solution (5 mL) of DPNDI ligands (0.0126 g, 0.03 mmol), and then an EtOH (5 mL) solution of $ZnSiF_6 \cdot 6H_2O$ (0.2 mmol, 0.041g) was carefully added as a third layer. Light-yellow crystals of Zn-NDI were obtained after remaining for several days in the dark (69% yield based on DPNDI). The obtained Zn-NDI was soaked in ethanol solution to stand for 5 days, and then the resulting materials were filtered, washed with ethanol and dried in *vacuo* at 80 °C.

2.3 Synthesis of Zn-NDI⊃TTF and Zn-NDI⊃Py

The synthetic approach for Zn-NDI⊃TTF and Zn-NDI⊃Py was similar to the procedure followed for Zn-NDI, with the difference in introducing the corresponding guest molecule (0.3 mmol) into the NMP solution of the DPNDI ligand. For Zn-NDI⊃TTF, dark-red crystals were obtained after several days. The yield of is ca. 62% based on DPNDI. For Zn-NDI⊃Py, red crystals were obtained after several days. The yield of is ca. 67% based on DPNDI.

3. Photothermal conversion properties measurement

The 100 mg material was pressed into 5-mm-diameter pellet using a manual tablet press at the pressure of 3.0 MPa. The obtained pellet was under continuous irradiation of an 808 nm laser until the sample reached a steady-state temperature. The temperature was monitored every 1 s by a Fluke (Ti400) thermal imaging camera. The 808 nm laser beam was irradiated at a power density from 0.1 to 0.9 $W \cdot cm^{-2}$.

4. DFT Computational details

All of the calculations were investigated with the Gaussian 16 software package (Gaussian 16, Revision C. 01; Gaussian, Inc., Wallingford CT, 2019). Structural optimizations and electronic properties were performed using the B3LYP functional with 6-31G(d, p) basis set (empirical dispersion correction GD3(BJ)). The structure is fully optimized, and a frequency calculation is performed to ensure that the optimized geometry corresponds to a true minimum (no imaginary frequencies). The single-point energy calculations are also carried out at the same level of theory. The charge distribution is analyzed based on the population analysis method, and the electrostatic potential is calculated and visualized to examine the distribution of the charge in the molecular system. The convergence criterion for the geometry optimization is set to 10^{-4} a.u. for the energy change, and the maximum force is set to 0.00045 a.u. to ensure accurate results.

5. Calculation of photothermal conversion efficiency

The conversion efficiency was determined according to previous method. Details are as follows:

$\eta = hS\Delta T_{max}/I(1 - 10^{-A})$

where I is the laser power and A is the absorbance of the samples at the wavelength of 808 nm. In order to obtain the hS, a dimensionless driving force temperature, θ is introduced as follows:

$\theta = (T - T_{surr}) / (T_{max} - T_{surr})$

T_{max} is the maximum system temperature, and T_{surr} is the initial temperature

$t = -\tau s \ln \theta$

τs could be calculated from the slope of cooling time vs ln θ.

6. The efficiency (η) of solar energy conversion

Photothermal-assisted water evaporation was calculated as the following formula

$\mu = m\ h_{LV} / Copt\ P_0$

Where: m = mass evaporation rate

h_{LV} = the total enthalpy of liquid-gas phase change, including sensible heat and vaporization enthalpy (h_{LV} =Q + Δvap)

Q = the energy required to heat the system from the initial temperature T_0 to the final temperature T

Δvap = latent heat of vaporization of water

$Copt$=optical concentration

P_0 = nominal solar radiation value, typically 1 kW m^{-2}.

7. Water evaporation performance under one simulated 1 sun light irradiation

For photothermal water evaporation performance testing, host−guest material powders (50 mg) are put on polyvinylidene fluoride (PVDF) membrane (Φ = 30 mm) tightly. Deionized water or brine (3.5% NaCl solution) was placed in a cylindrical beaker with a mouth diameter of 3.0 cm, and the membrane with the host−guest material powders was put and self-floated on the top of water. The sun solar light irradiation (1000 W/m^2) was illuminated from the top and onto the surface of the host−guest material powders vertically. the temperature of the host−guest material powders was recorded by IR camera and the mass of the water evaporated was real time monitored by a digital balance.

8. Calculation of the water evaporation efficiency under simulated 1 sun light irradiation.

The water evaporation rate was calculated by the following equation:

$$v = \frac{dm}{S \times dt}$$

Where m is the mass of evaporated water, S is the illuminated area, t is time, and ν is evaporation rate.

In the end, light to water evaporation efficiency was calculated based on following equation:

$$Q_e = \frac{dm \times h_e}{dt} = v \times h_e$$

$$\text{evaporation efficiency} = \frac{Q_e}{Q_s}$$

Where Q_e is energy consumed for water evaporation, Q_s is the incident simulated solar light power, m is the mass of evaporated water recorded by the balance, and H_e is the enthalpy of vaporization of water.

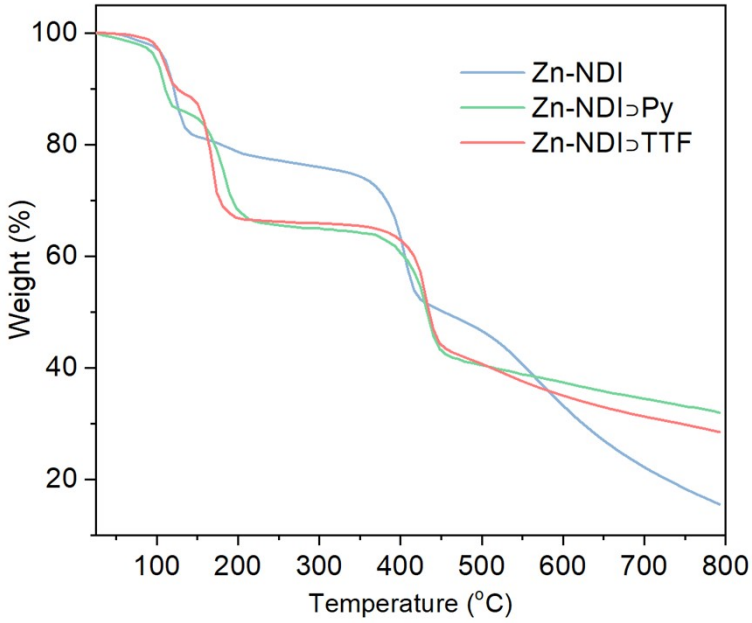

Fig. S1. TGA curves of Zn-NDI, Zn-NDI⊃Py, and Zn-NDI⊃TTF.

Table S1. Weight loss and Calculated formula of Zn-NDI⊃Py and Zn-NDI⊃TTF.

Sample	Weight loss in the 125-250 °C	Calculated formula
Zn-NDI⊃Py	20.4%	$Zn(DPNDI)_2SiF_6 \cdot 1.33Py$
Zn-NDI⊃TTF	23.5%	$ZnSiF_6(DPNDI)_2 \cdot 1.57TTF$

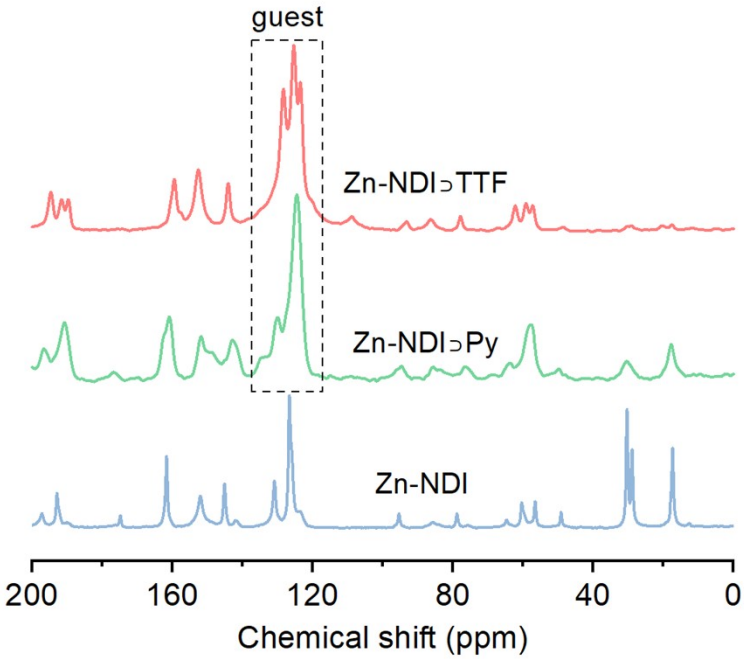

Fig. S2. Solid-state ^{13}C NMR spectra of Zn-NDI, Zn-NDI⊃Py, and Zn-NDI⊃TTF.

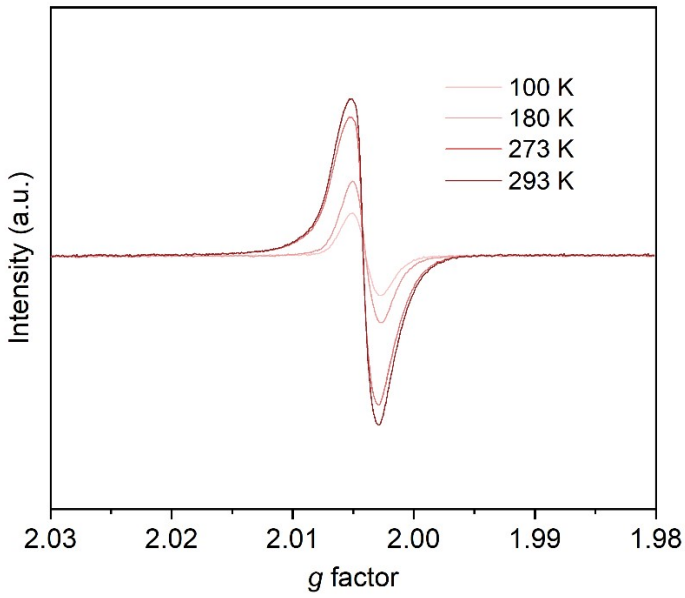

Fig. S3. VT-ESR spectra of Zn-NDI⊃Py.

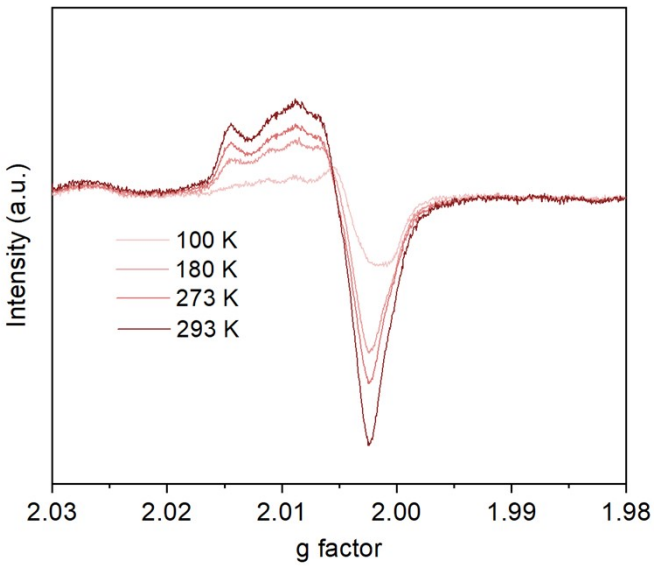

Fig. S4. VT-ESR spectra of Zn-NDI⊃TTF.

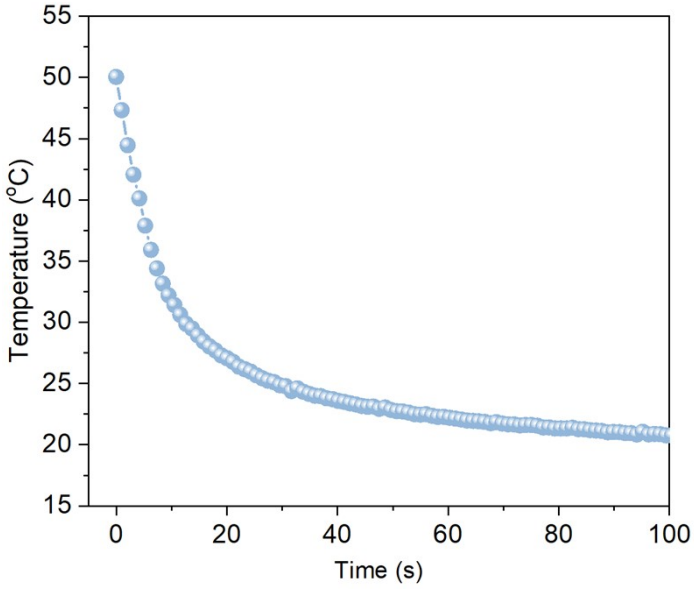

Fig. S5. The cooling curve of Zn-NDI film after irradiation with 808 nm laser (0.7 W·cm^{-2}).

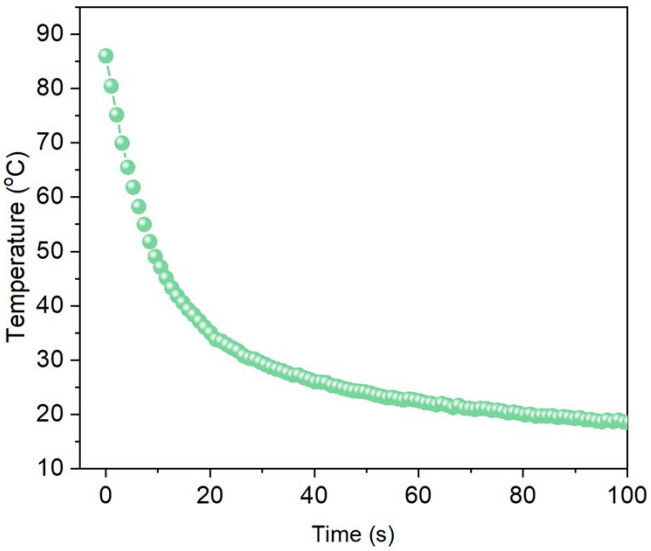

Fig. S6. The cooling curve of Zn-NDI⊃Py film after irradiation with 808 nm laser (0.7 W·cm^{-2}).

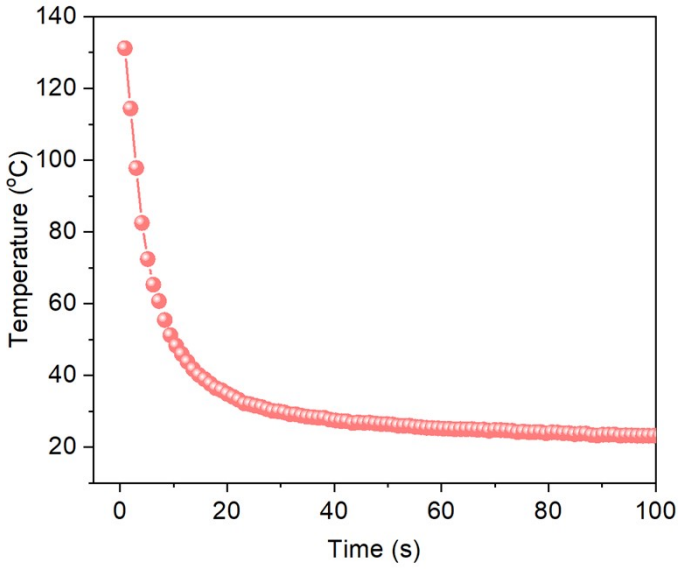

Fig. S7. The cooling curve of Zn-NDI⊃TTF film after irradiation with 808 nm laser (0.7 W·cm^{-2}).

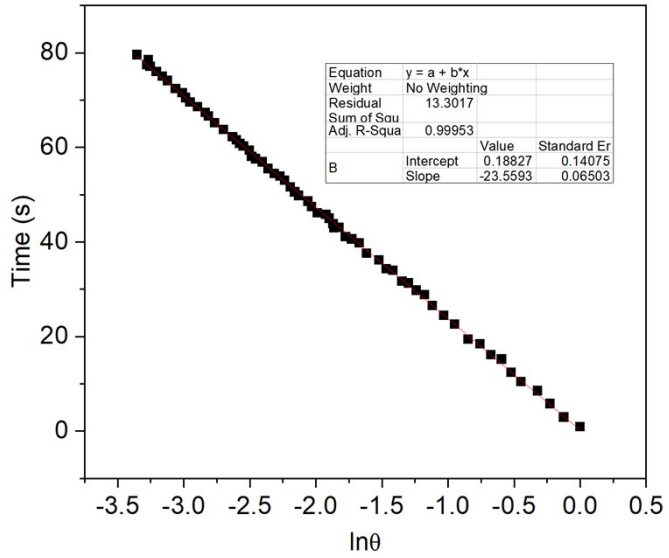

Fig. S8 The time-lnθ linear curve of Zn-NDI.

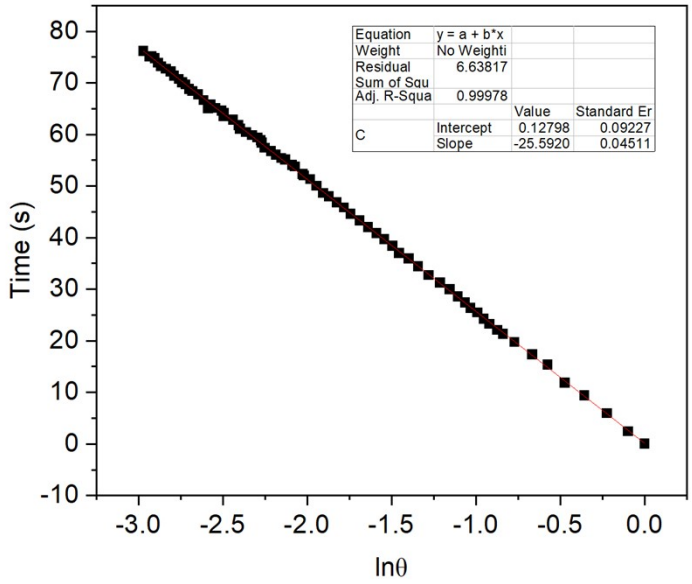

Fig. S9 The time-lnθ linear curve of Zn-NDI⊃Py.

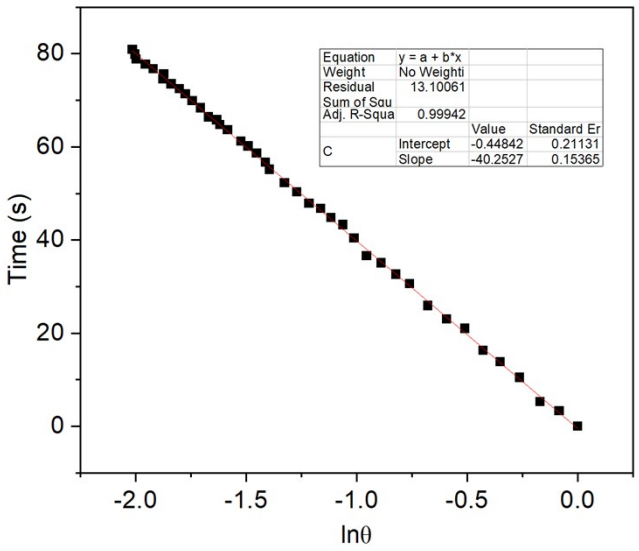

Fig. S10 The time-lnθ linear curve of Zn-NDI⊃TTF.

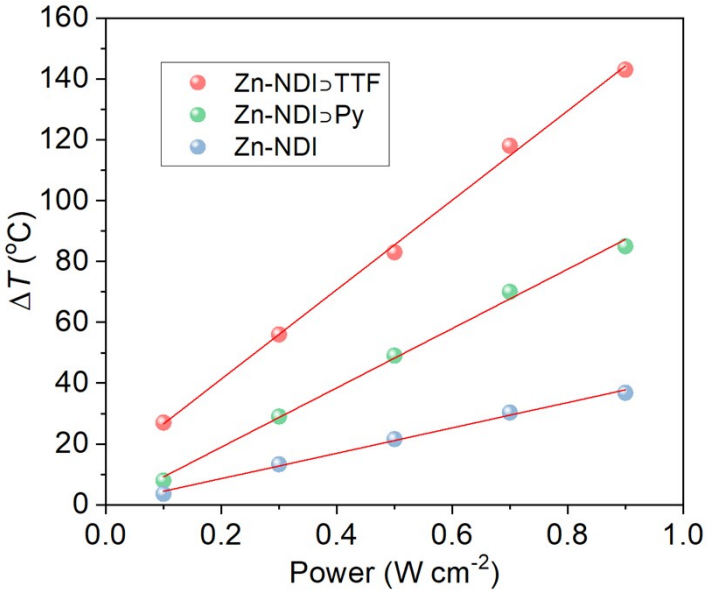

Fig. S11. Plot of average temperature rise (ΔT) against power density of 808 nm laser.

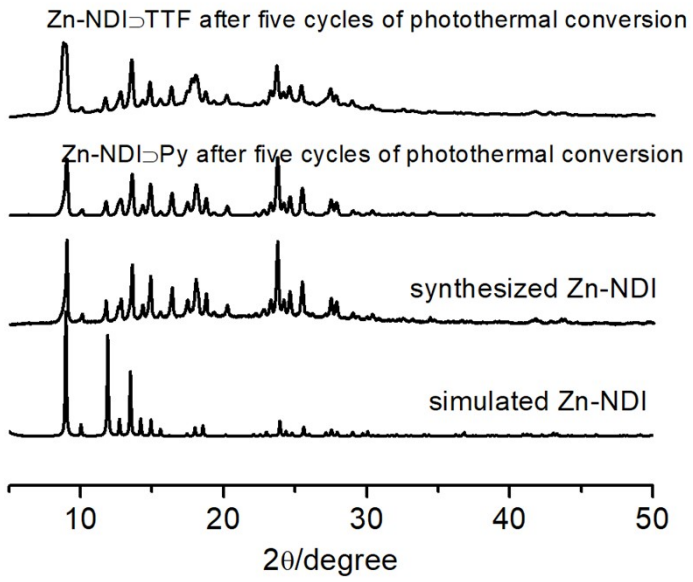

Fig. S12. PXRD patterns of Zn-NDI⊃Py and Zn-NDI⊃TTF after five cycles of photothermal conversion.

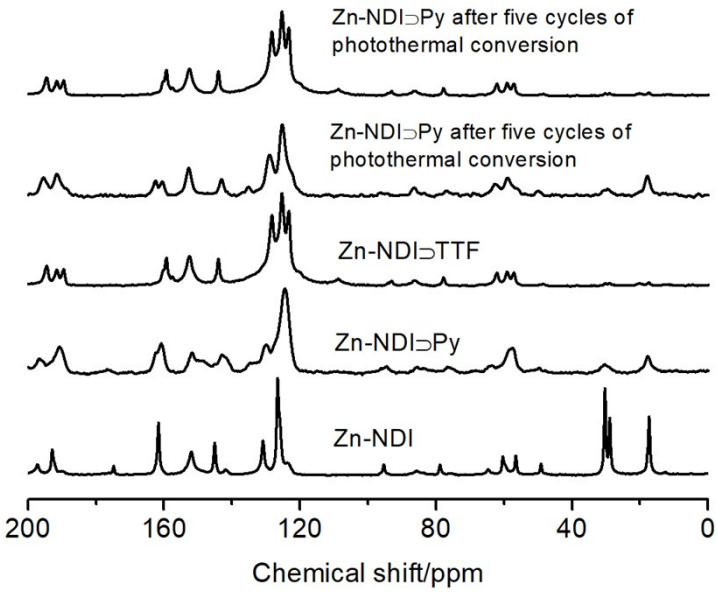

Fig. S13. Solid-state ^{13}C NMR spectra of Zn-NDI⊃Py and Zn-NDI⊃TTF after five cycles of photothermal conversion.

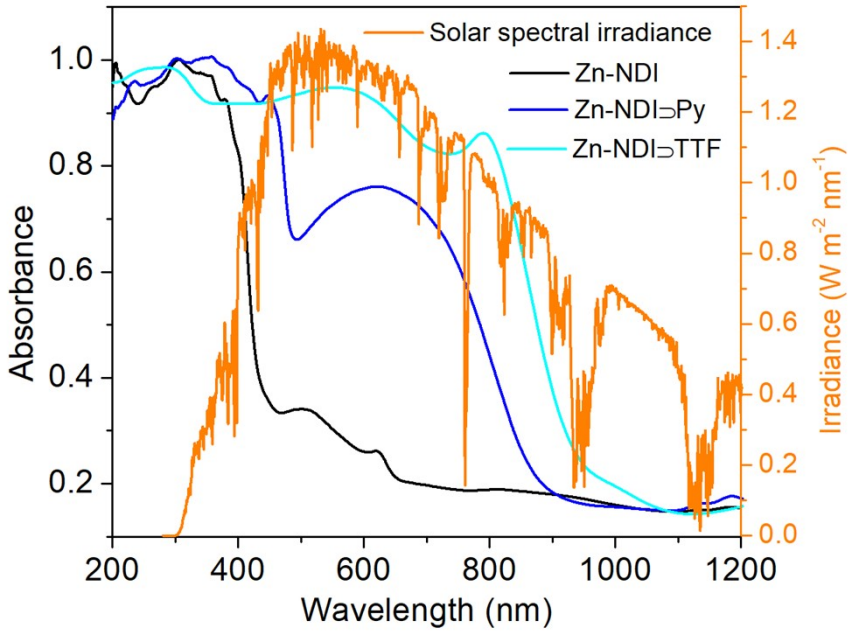

Fig. S14. UV-Vis-NIR spectra of Zn-NDI, Zn-NDI⊃TTF, Zn-NDI⊃Py, and referenced standard solar spectral irradiance.

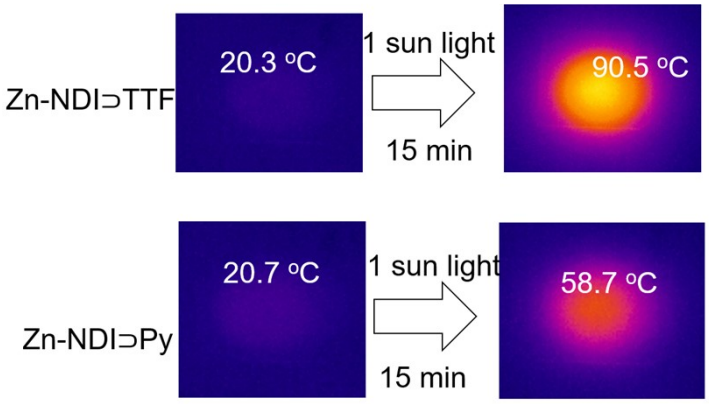

Fig. S15. IR thermal images of the surface temperature of Zn-NDI⊃TTF and Zn-NDI⊃Py during the water evaporation experiments.

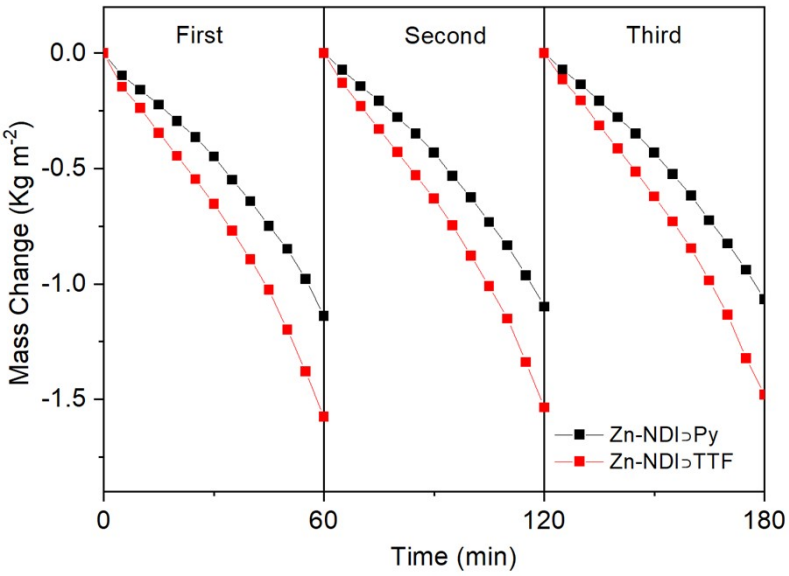

Fig. S16. Cycling water evaporation experiments under simulated 1 sun light irradiation.

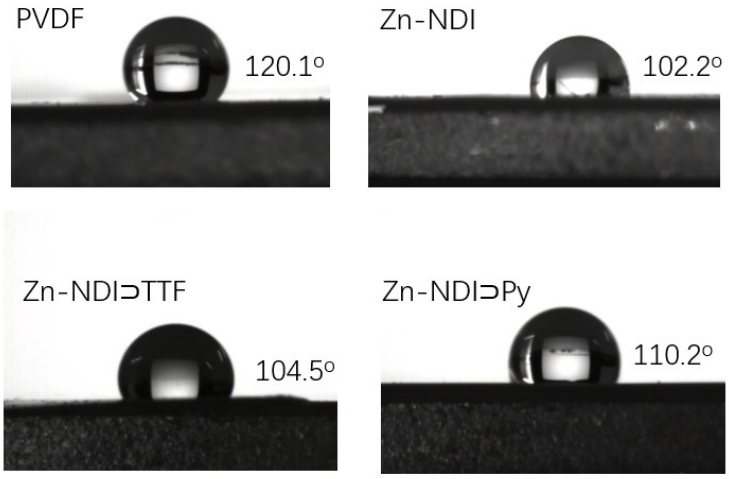

Fig. S17. The contact angles of PVDF, Zn-NDI, Zn-NDI⊃TTF, and Zn-NDI⊃Py with water at room temperature.

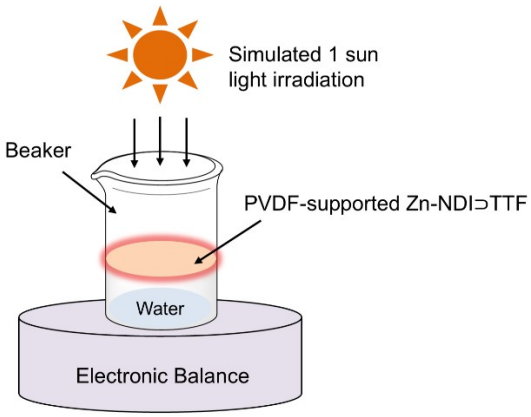

Fig. S18. Simple schematic diagram of water evaporation device.

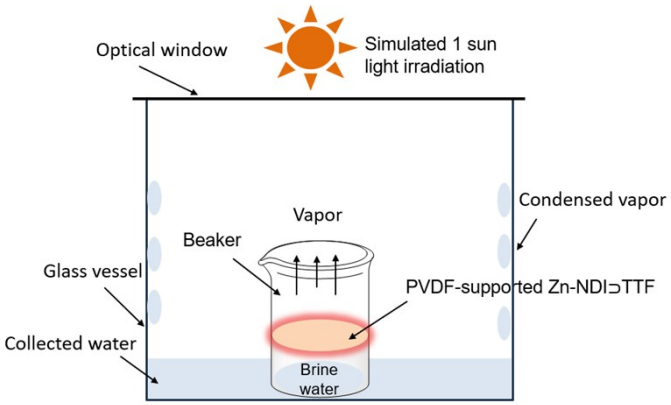

Fig. S19. Diagram of the solar-driven water evaporation measurement.

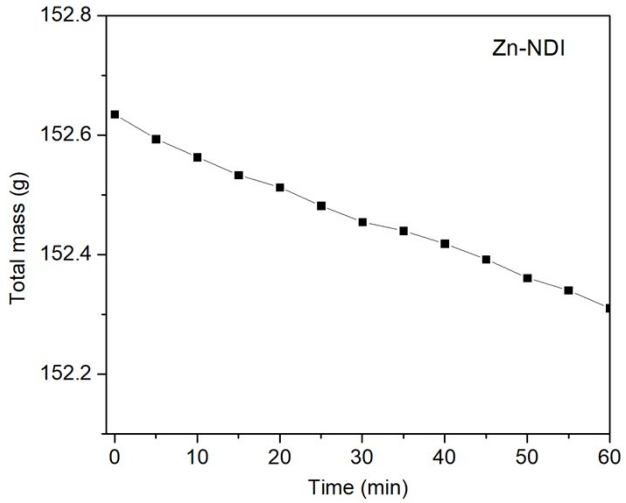

Fig. S20. Raw mass-loss curve of water evaporation using Zn-NDI as photothermal conversion material under simulated 1 sun light irradiation (the diameter of the material is 3 cm).

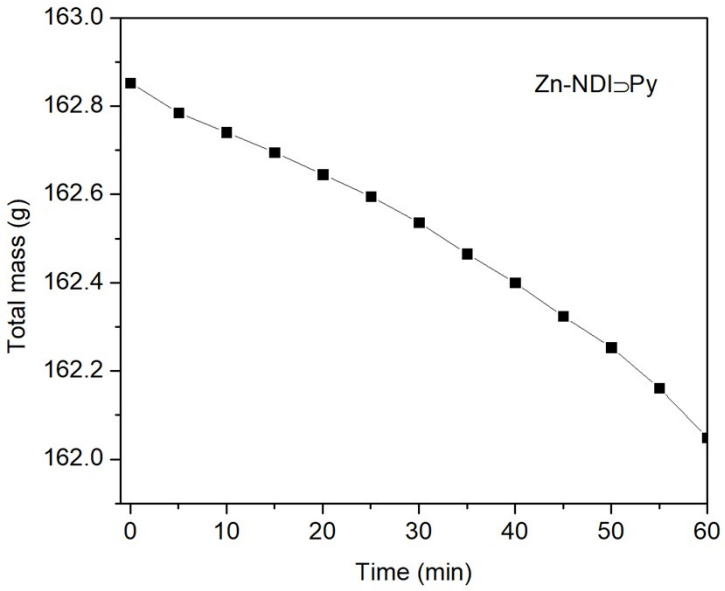

Fig. S21. Raw mass-loss curve of water evaporation using Zn-NDI⊃Py as photothermal conversion material under simulated 1 sun light irradiation (the diameter of the material is 3 cm).

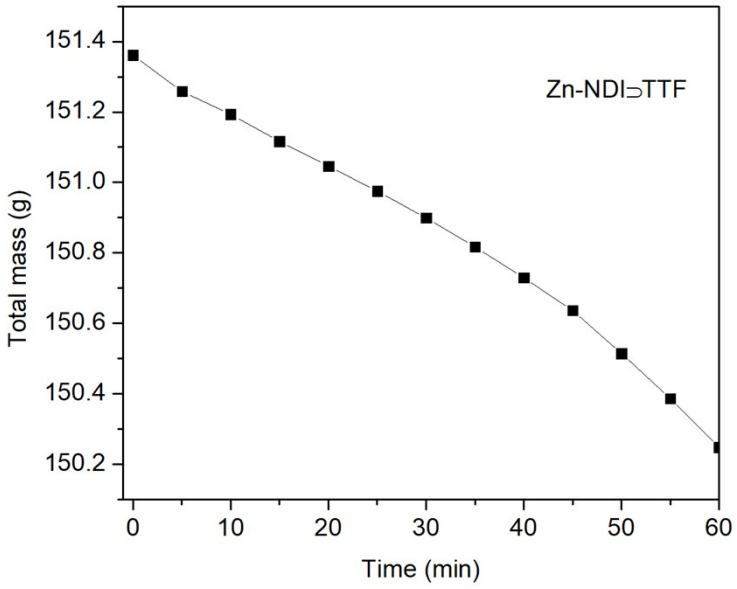

Fig. S22. Raw mass-loss curve of water evaporation using Zn-NDI⊃TTF as photothermal conversion material under simulated 1 sun light irradiation (the diameter of the material is 3 cm).

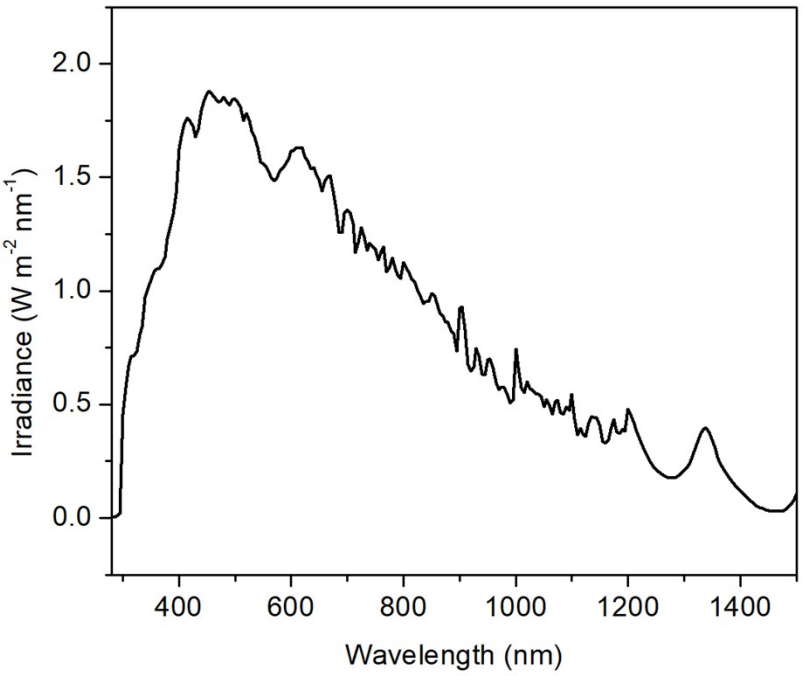

Fig. S23. Simulated solar irradiance data for photothermal water evaporation experiments.

Table S2. The NIR photothermal properties in this work compared with previous results of solid materials in the literatures

Samples	Added temperature	Power ($W \cdot cm^{-2}$)	NIR laser source	Pretreatment	Ref.
Co-MOF	176	0.7	808 nm	None	[S3]
Rb-NDI	83	1.6	808 nm	Blue light irradiation	[S4]
HPTS	75	0.8	808 nm	Blue light irradiation	[S5]
La-bcbp	120	2	808 nm	UV-vis irradiation	[S6]
Zr-PDI$^{\bullet-}$	141	1	808 nm	TEA vapor fumigation blue light irradiation	[S7]
PMDI-TTF co-crystal	70	0.7	808 nm	None	[S8]
DTC- co-crystal	45	0.7	808 nm	None	[S9]
CR-TPE-T	103	1.2	808 nm	None	[S10]
Ag-CP	25	0.5	808 nm	None	[S11]
EuMo-NDI	81.7	1.0	808 nm	UV-vis irradiation	[S12]
RhB@Cd-pbc	78	0.9	808 nm	None	[S13]
$Cu_{48}S_{30}$ cage	90.3	1	808 nm	None	[S14]
Au@MOF	55.1/73.5	0.8/1.8	808/1064 nm	Au Nanostar@MOF	[S15]
Cu-THQNPs	22.1/45	1.0/2.0	808/1064 nm	PEG-$(NH_2)_2$	[S16]
TTFDPNI-CdMOF	254	0.7	808 nm	None	[S17]
TTFDPNI-CoMOF	230	0.7	808 nm	None	[S17]
MOF 1	129/137	0.5	808/1064 nm	None	[S18]
TTF@MOFL7	38.6	1.19	808 nm	None	[S19]
CP-TCNQ	58.1	0.91	808 nm	None	[S20]
D289-F4TCNQ	60.1	0.69	808 nm	None	[S21]
Zn-NDI⊃TTF	118.2	0.7	808 nm	None	This work
Zn-NDI⊃Py	70.4	0.7	808 nm	None	This work

Table S3. Performance metrics of reported materials for solar-driving water evaporation.

Samples	Water evaporation rate (kg m^{-2} h^{-1})	Solar-to-vapor efficiency	Ref.
CoTCPP-Bi	1.43	98.5	S22
EuTTA-350	1.44	97.9	S23
PDANWs-NF	1.39	87.8	S24
OR-R-CF	1.36	85.3	S25
MNM@PVDF/SA	1.34	90.6	S26
Cu-CAT-1	1.50	97.6	S27
TPA-TPA-O6	1.29	89.4	S28
Ni3S2@NF	1.53	84.5	S29
HKUST-1/SWCNT	1.38	90.3	S30
TTFDPNI-Cd-MOF	1.78	96.8	S31
Tri-PMDI@TTF	1.77	46.2	S32
Zn-NDI⊃TTF	1.75	91.3	This work
Zn-NDI⊃Py	1.23	82.6	This work

References

[S1] Guha, S.; Goodson, F. S.; Corson, L. J.; Saha, S. Boundaries of Anion/Naphthalenediimide Interactions: From Anion−π Interactions to Anion-Induced Charge-Transfer and Electron-Transfer Phenomena. J. Am. Chem. Soc. 2012, 134, 13679-13691.

[S2] Liu, J.-J.; Hong, Y.-J.; Guan, Y.-F.; Lin, M.-J.; Huang, C.-C.; Dai, W.-X. Lone pair–π interaction-induced generation of non-interpenetrated and photochromic cuboid 3-D naphthalene diimide coordination networks. Dalton Trans. 2015, 44, 653-658.

[S3] Yan, T.; Li, Y. Y.; Su, J.; Wang, H. Y.; Zuo, J. L. Charge Transfer Metal-Organic Framework Containing Redox-Active TTF/NDI Units for Highly Efficient Near-Infrared Photothermal Conversion. Chem.-Eur. J. 2021, 27, 11050−11055.

[S4] Ke, H.; Zhu, X.-M.; Xie, S.-M.; Ming, P.-X.; Liao, J.-Z. Ultrastable Radicals in Naphthalenediimide-Based Materials and Their Stimulus-Boosting Near-Infrared Photothermal Conversion. Inorg. Chem. Front. 2022, 9, 2568–2574.

[S5] Liao, J.-Z.; Liu, S.-J.; Ke, H. Excited-State Proton Transfer in a Photoacid-Based Crystalline Coordination Compound: Reversible Photochromism, Near-Infrared Photothermal Conversion, and Conductivity. Inorg. Chem. 2023, 62, 16825–16831.

[S6] Wang, S.; Li, S.; Xiong, J.; Lin, Z.; Wei, W.; Xu, Y. Near-Infrared Photothermal Conversion of Stable Radicals Photoinduced from a Viologen-Based Coordination Polymer. Chem. Commun. 2020, 56, 7399–7402.

[S7] Lü, B.; Chen, Y.; Li, P.; Wang, B.; Müllen, K.; Yin, M. Stable Radical Anions Generated from a Porous Perylenediimide Metal-Organic Framework for Boosting Near-Infrared Photothermal Conversion. Nat. Commun. 2019, 10, 767.

[S8] Wang, D.; Kan, X.; Wu, C.; Gong, Y.; Guo, G.; Liang, T.; Wang, L.; Li, Z.; Zhao, Y. Charge transfer co-crystals based on donoracceptor interactions for near-infrared photothermal conversion. Chem. Commun. 2020, 56, 5223-5226.

[S9] Tian, S.; Huang, Z.; Tan, J.; Cui, X.; Xiao, Y.; Wan, Y.; Li, X.; Zhao, Q.; Li, S.; Lee, C.-S. Manipulating Interfacial Charge-Transfer Absorption of Cocrystal Absorber for Efficient Solar Seawater Desalination and Water Purification. ACS Energy Lett. 2020, 5, 2698–2705.

[S10] Chen, G.; Sun, J.; Peng, Q.; Sun, Q.; Wang, G.; Cai, Y.; Gu, X.; Shuai, Z.; Tang, B. Z. Biradical-Featured Stable Organic-Small Molecule Photothermal Materials for Highly Efficient Solar-Driven Water Evaporation. Adv. Mater. 2020, 32, 1908537.

[S11] Li, M.-Q.; Zhao, M.; Bi, L.-Y.; Hu, Y.-Q.; Gou, G.; Li, J.; Zheng, Y.-Z. Two-Dimensional Silver(I)-Dithiocarboxylate Coordination Polymer Exhibiting Strong Near-Infrared Photothermal Effect. Inorg. Chem. 2019, 58, 6601-6608.

[S12] Chen, S.; Yang, Q.; Shen, X.; Cheng, F.; Liu, J.-J. Naphthalenediimide-Based Hybrid Material with Eu-Substituted Polyoxometalate: Photochromism, Near-Infrared Photothermal Conversion, and C-3 Functionalization of Indoles. Inorg. Chem. 2025, 64, 3008–3016.

[S13] Yang, X.-D.; Lv, H.; Dong, W.; Wen, Y.; Fu, M.; Zhang, Q.; Zhou, L.; Xuan, X. Recycling Organic Dyes within the Metal–Organic Framework for Photothermal Conversion. Inorg. Chem. 2024, 63, 13714–13723.

[S14] Yan, B.; Sun, J.; Liu, J.; Li, L.; Deng, H.; Xu, Q.; Wang, S.; Shen, H. Flat-Shaped Copper Nanoclusters with Near-Infrared Absorption for Enhanced Photothermal Conversion. JACS Au 2025, 5, 1884–1893.

[S15] Deng, X.; Liang, S.; Cai, X.; Huang, S.; Cheng, Z.; Shi, Y.; Pang, M.; Ma, P.; Lin, J. Yolk–Shell Structured Au Nanostar@Metal-Organic Framework for Synergistic Chemo-Photothermal Therapy in the Second Near-Infrared Window. Nano Lett. 2019, 19, 6772–6780.

[S16] Liao, J.-Z.; Jiang, Y.; He, F.-F.; Jiang, L.-L.; Zhu, X.-M.; Ke, H. Photo-Induced Organic Radical Species in Naphthalenediimide-Based Metal-Organic Framework for Reversible Photochromism and Near-Infrared Photothermal Conversion. Mater. Today Chem. 2023, 27, 101324.

[S17] Zheng, X.-Y.; Wang, C.; Luo, X.-F.; Su, J.; Xiao, X. Tuning Donor−Acceptor Stacking in MOFs via Rational Metal Coordination for Enhanced Photothermal Conversion and Solar Driven Water Evaporation Performance. Inorg. Chem. 2025, 64, 19369–19376.

[S18] Chen, S.; Zeng, H.; Kong, C.; Cheng, F.; Liu, J.-J. Pyromellitic Diimide-Based Donor−Acceptor MOF with Panchromatic Absorption for High-Efficiency Photothermal Conversion. Inorg. Chem. 2025, 64, 19916−19923.

[S19] E. Hernández-Santiago, A. Navarro-Huerta, V. Gómez-Vidales, J. Rodríguez-Hernández, M. Rodríguez, J. D. Evans, B. Rodríguez-Molina, A Host−Guest Approach to Generate a Zr-Based MOF with Photothermal Conversion Properties. ACS Appl. Opt. Mater. 2025, 3, 1237−1244.

[S20] Navarro-Huerta, A.; Hall, D. A.; Blahut, J.; Gómez-Vidales, V.; Teat, S. J.; Marmolejo-Tejada, J. M.; Dračínský, M.; M. Mosquera, A.; Rodríguez-Molina, B. Influence of Internal Molecular Motions in the Photothermal Conversion Effect of Charge-Transfer Cocrystals. Chem. Mater. 2023, 35, 10009–10017.

[S21] S.-L. Chen, M.-M. Zhang, J. Chen, X. Wen, W. Chen J. Li, Y.-T. Chen, Y. Xiao, H. Liu, Q. Tan, T. Zhu, B. Ye, J. Yan, Y. Huang, J. Li, S. Ni, L. Dang, M.-D. Li, Mechanochemistry toward Organic “Salt” via IntegerCharge-Transfer Cocrystal Strategy for Rapid, Efficient, and Scalable Near-Infrared Photothermal Conversion. ChemSusChem 2023, 16, e202300644.

[S22] He, L.; He, J.; Chen, E.; Lin, Q. Boosting photothermal conversion through array aggregation of metalloporphyrins in bismuth-based coordination frameworks. Chem. Sci. 2024, 15, 17498.

[S23] Ye, X.; Chung, L.; Li, K.; Zheng, S.; Wong, Y.; Feng, Z.; He, Y.; Chu, D.; Xu, Z.; Yu, L.; He, J. Organic radicals stabilization above 300 °C in Eu-based coordination polymers for solar steam generation. Nat. Commun. 2022, 13, 6116.

[S24] Ibrahim, I.; Hossain, S.; Seo, D.; McDonagh, A.; Foster, T.; Shon, H.; Tijing, L. Insight into the role of polydopamine nanostructures on nickel foam-based photothermal materials for solar water evaporation. Sep. Purif. Technol. 2022, 293, 121054.

[S25] Zhao, S.; Xia, M.; Zhang, Y.; Hasi, Q.; Xu, J.; Chen, L. Novel oil-repellent photothermal materials based on copper foam for efficient solar steam generation. Sol. Energy Mater. Sol. Cells 2021, 225, 111058.

[S26] Wang, J.; Zhao, Z.; Yang, C.; Sun, M.; Chen, J.; Zhou, Y.; Xu, H. Marine biomass metal-organic framework hybrid evaporators for efficient solar water purification. Desalin. 2023, 556, 116577.

[S27] Ma, Q.; Yin, P.; Zhao, M.; Luo, Z.; Huang, Y.; He, Q.; Yu, Y.; Liu, Z. MOF-Based Hierarchical Structures for Solar-Thermal Clean Water Production. Adv. Mater. 2019, 31, 1808249.

[S28] Wang, Z.; Zhou, J.; Zhang, Y.; Zhu, W.; Li, Y. Accessing Highly Efficient Photothermal Conversion with Stable Open-Shell Aromatic Nitric Acid Radicals. Angew. Chem. Int. Ed. 2022, 61, e202113653.

[S29] Yao, Z.; Yu, K.; Pan, M.; Xu, H.; Zhao, T.; jiang, Z. A mechanically durable, excellent recyclable 3D hierarchical Ni_3S_2@Ni foam photothermal membrane. Green Energy Environ. 2022, 7, 492-499.

[S30] Peng, X.; Ma, X.; Fang, W.; Guo, Y.; Li, Z.; Chen, D.; Ying, W.; Xu, Z.; Gao, C. Hierarchical Porous SWCNT Stringed Carbon Polyhedrons and PSS Threaded MOF Bilayer Membrane for Efficient Solar Vapor Generation. Small 2019, 15, 1900354.

[S31] Zheng, X.-Y.; Wang, C.; Luo, X.-F.; Su, J.; Xiao, X. Tuning Donor–Acceptor Stacking in MOFs via Rational Metal Coordination for Enhanced Photothermal Conversion and Solar-Driven Water Evaporation Performance. Inorg. Chem. 2025, 64, 19369–19376.

[S32] Wang, D.; Kan, X.; Wu, C.; Gong, Y.; Guo, G.; Liang, T.; Wang, L.; Li, Z. Charge transfer co-crystals based on donor–acceptor interactions for near-infrared photothermal conversion. Chem. Commun., 2020,56, 5223-5226.